

D-SEAMS: DEFERRED STRUCTURAL ELUCIDATION ANALYSIS FOR MOLECULAR SIMULATIONS

A PREPRINT

 **Rohit Goswami***

Department of Chemical Engineering
Indian Institute of Technology Kanpur
rgoswami@iitk.ac.in

 **Amrita Goswami†**

Department of Chemical Engineering
Indian Institute of Technology Kanpur
amritag@iitk.ac.in

 **Jayant K. Singh‡**

Department of Chemical Engineering
Indian Institute of Technology Kanpur
jayantks@iitk.ac.in

January 1, 2023

ABSTRACT

d-SEAMS is an open-source, community supported engine for the analysis of molecular dynamics trajectories. Our framework leverages functional nix-language expressions for generating deterministic dependency build graph with cryptographic hashes. Workflows are exposed to the user via intuitive text-based interfaces using YAML options. A Lua scripting interface exposes low-level API functionality for generating new pipelines and modifying existing workflows. The engine outputs are immediately consumable by popular graphics software suites, allowing for immediate visual insights into the systems studied. Molecular mechanisms can be inferred from the time evolution of the d-SEAMS structure analysis routines. We apply the workflows to analyze nucleation in the bulk regime and for quasi-one and quasi-two-dimensional systems. Structural time evolution and quantitative metrics are determined for heterogeneous ice nucleation on a silver-exposed β -AgI surface, homogeneous ice nucleation, flat monolayer square ice formation and freezing of an ice nanotube.

Keywords structure-determination, analysis-engine, computational-chemistry, nix, lua, cpp

1 Introduction

Water is a deceptively simple molecule, exhibiting rich and complex phase behaviour in bulk and confinement [1–11]. At least 17 bulk ice polymorphs have been observed experimentally [12, 13]. Water confined within nanometer length scales exhibits even more diversity, forming ordered hydrogen-bond networks of ice nanotubes, monolayers, bilayers and trilayers [9, 14–20]. The structural determination of the several possible polymorphs of water, in bulk and in confinement, is of crucial importance in the qualitative and quantitative analysis of simulation data. The time evolution of ordered structures can also reveal the underlying mechanism of the nucleation process and provide physical insights into the system.

In this work, we present d-SEAMS, a cohesive post-processing structural analysis engine, which is capable of coherently classifying water structures across scales, from quasi-one and two-dimensional confinement to bulk ice polymorphs. In particular, confined ice polymorphs are often identified “by eye” wherein the hydrogen-bond network (HBN) is

*Currently at the Department of Chemistry, IIT Kanpur, *equal contribution*

†*equal contribution*

‡**Corresponding Author**

manually inspected [9, 11, 18]. d-SEAMS automates the process of structural analysis and qualitative metric calculation, eliminating the need for visual inspection.

Conflicting package clashes due to transitive or indirect dependencies is a recurring problem in software development and use [21]. Most of the post-processing scientific softwares available are implemented as python libraries [22–24]. Python libraries can be particularly susceptible to cyclic build dependencies and conflicts [25, 26]. Resolving such issues can often be non-trivial, relying on removal of unnecessary dependencies, system updates (for most Linux clusters) and other manual strategies that may be ineffective for a complex dependency tree. These manual strategies are increasingly difficult to carry out on restricted access machines with high up-times which are common to the HPC (High Performance Computing) clusters used for such simulations.

d-SEAMS circumvents the problem of ‘dependency hell’ by using `nix` [27] for generating reproducible dependency build-graphs [28]. Users can run d-SEAMS using the exact build-environment of the developers and vice-versa, bypassing installation and use issues on various systems and HPC clusters, ensuring reproducible research.

d-SEAMS has been designed to permit easy extensions to the code and the implementation of custom work-flows. The engine simultaneously incorporates user-friendly interface functions without compromising on functionality. Key features implemented include a primitive ring analysis algorithm [29], topological network criteria for bulk [30] and confined systems [31] and new qualitative order parameters. Outputs are produced in formats compatible with popular visualization softwares, including OVITO [32] and VMD [33]. We describe applications of analyses performed by d-SEAMS in analyzing and characterizing ice nucleation on an ice-promoting AgI surface, homogenous bulk nucleation, the formation of monolayer ice and the freezing of a quasi-one-dimensional ice nanotube (INT).

2 Design

The d-SEAMS framework is designed to be accessible to the end-user, while offering a powerful system of building blocks and generics for extensions. The engine itself is written in C++ and is compiled to a binary. This binary accepts Lua input scripts to expose the functionality of the software such that the underlying data-structures and computations are abstracted away from the user. To facilitate reproduction of results and to prevent users from accessing conflicting or unphysical functional manipulations of the input data, YAML options mask certain functions from being exposed. The YAML workflows are completely reproducible in Lua scripts, but provide an easy way to share methodologies and also reduces the cognitive load of going through the complete API documentation.

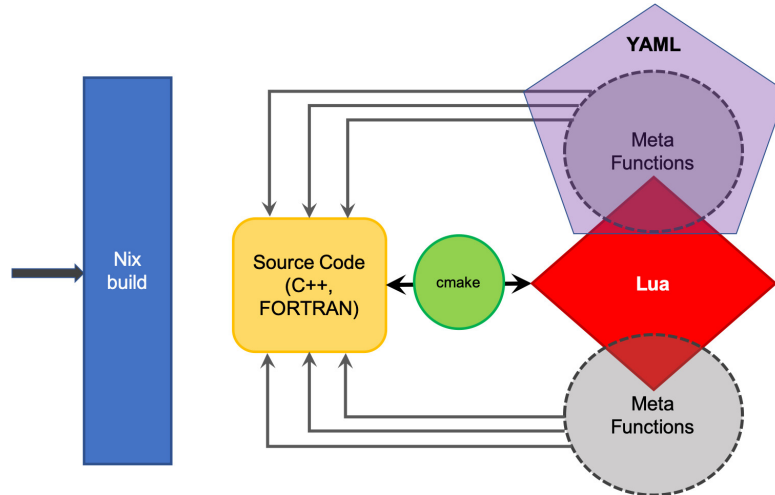


Figure 1: Work-flow of d-SEAMS. ‘Nix’ uses cryptographic hashes to ensure reproducible builds over all systems. ‘Cmake’ compiles and builds the source code, using the dependencies managed by ‘nix’. The ‘Lua’ script provides an interface to the back-end functions. Combinations of these ‘C++’ functions can be called the ‘meta’ functions. The ‘YAML’ interface exposes only relevant back-end and ‘Lua’ functions, corresponding to the user-determined pre-determined work-flow.

Figure 1 is a schematic of the overall design architecture of d-SEAMS. The Lua scripting interface exposes C-like functions to create custom work-flows. The YAML configuration file provides options for pre-determined work-flows.

Users with different requirements and experience can interact with d-SEAMS. The three main components of the code architecture are enumerated below:

- **YAML configuration file:** This contains options for pre-determined work-flows. For example, a user who enters the option for the confined quasi-one-dimensional ice determination will only be exposed to the relevant functions for INT prism determination. Multiple workflows can be selected at the same time.
- **Lua Interface:** C++ functions are registered as Lua functions, which are called from a Lua script. Lua is a C-like scripting language, enabling users to call the Lua functions without needing to learn a software-specific scripting convention. The advantage of using Lua over directly calling C++ functions is that the users need not be concerned with pointers and clean-up of the C++ structures. The Lua language also has a rich set of cross platform extensions for file handling, and is also supported by major editors for syntax highlighting.
- **C++ Back-end:** The back-end is written in modern C++, employing common data structures, used uniformly throughout the code. Users can easily extend and write their own C++ header files, and the documentation covers manipulating the build system to accept both user-defined and external headers. Registering custom C++ functions as Lua functions, to be subsequently called in Lua scripts, is also documented. GDB [34] can be used for code debugging, since the back-end is in C++.

2.1 Nix

Computational software implemented in declarative package management systems suffer from design concerns for the end-users and the developers. The developers have the onus to package their software as per the many imperative systems (Ubuntu and apt, RedHat and yum, ArchLinux and pacman). Additionally, the users must ensure that the interrelated dependencies match perfectly (as in the case of python distributions). In essence, the issue is that the packages and versions at the time of build are not guaranteed automatically at the user’s end, even if the software is packaged appropriately for the operating system. This issue stems from the fact that the configuration after installation is the result of a series of stateful transformations which cannot be reproduced [35]. We have opted to package our software as a nix-derivation [27], which also provides a functionally reproducible environment for reproducible bug-tests. The derivation provides a deterministic package-level lock on all dependencies and is written in nix, a lazy, dynamically typed, purely functional language [35]. This choice of distribution also allows the user to extend the system reproducibly, ensuring that changes can be quickly merged in-to the upstream repository. Since the build system is essentially a static graph of build actions, the environment produced (with nix-shell) is a boon for reproducible research, avoiding circular build-time dependencies and incomplete dependency specifications [36].

2.2 Lua

Existing molecular dynamics packages suffer from not having design parameters built-in, and with time, this has led to unique and non-standard syntax being used, as seen in the input scripts of LAMMPS [37] and GROMACS [38], amongst others. Popular text editors do not offer syntax highlighting for these custom non-standard and software-specific syntaxes. For such software-specific syntaxes, the code is unusable without learning from the documentation. An alternative to crafting a new input script syntax for each software, is to use python for scripting [39]. However, the version dependence of each internal segment can become intractable without continuous development, and as a result, these spawn multiple language-specific errors, and they work best only on the Linux distribution on which the creators have worked. Furthermore, we assert that the proliferation of python scripts and the odd-ease at which they may be, in theory mixed and matched, in practice causes many clashes, for example, EsPreSSo [40] and Quantum EsPreSSo [41] (and more generally, Scipy [42] and Numpy [43]) have several function names in common which cause difficult to debug when used together in an input script. Also, python has less support for debugging, and the language server support is lacking, making complex python code difficult to debug. This is partially due to the design of python itself. The lack of static typing has the effect of making the compiler oblivious to bugs which are caught easily in statically typed languages like FORTRAN and C++.

To address these concerns we have opted to use Lua as the scripting interface, which has C-like functions. It is widely supported in terms of syntax highlighting, and is easy to interface with C++ code. Furthermore, the error handling is such that it is amenable for arbitrarily complex GDB debugger workflows [44], and the rich standard library of Lua, along with user extensions, have no clashes. Lua is also user friendly due to its C-like syntax. The rich table and object handling makes writing out image data easy. Furthermore, though Lua was released two years after python was first introduced (1993 and 1991, respectively) unlike python, which is still transitioning from the major API change of two to three, the Lua API is stable, mostly because it has been designed to be an embedded language and not a general-purpose language like python. Lua has been the darling of the gaming development community, and has proven its worth in many related domains such as image handling. Apart from the user-friendly helper functions, our design

has the Lua interface, which offers every core function to the user. This permits arbitrarily complicated workflows to be used without re-compilation, which is a boon for HPC cluster usage. We recommend strongly in the docs, that foreign code, once interfaced to the C++ engine, should be bound in Lua for the end-users as well.

```

1  print("\n Welcome to the manual lua function evaluation environment.\n");
2
3  --- Init Modules
4  local lfs = require"lfs"
5
6  --- Call functions defined in script file
7  package.path = '../lua_inputs/luamodules/?.lua;' .. package.path
8  local luaFunctions = require("scripts");
9
10 --- Make the directories
11 luaFunctions.make_output_dirs( doBOP, topoOneDim, topoTwoDim, topoBulk );
12
13 for frame=targetFrame,finalFrame,frameGap do
14     --- Get the frame
15     resCloud=readFrameOnlyOne(trajjectory,frame,resCloud,oxygenAtomType,isSlice,
16                               sliceLowerLimits,sliceUpperLimits)
17     --- Calculate the neighborlist
18     nList=neighborList(cutoffRadius, resCloud, oxygenAtomType);
19     --- Get the hydrogen-bonded network for the current frame
20     hbnList=getHbondNetwork(trajjectory,resCloud,nList,frame,hydrogenAtomType)
21     hbnList=bondNetworkByIndex(resCloud,hbnList)
22     --- Gets every ring (non-primitives included)
23     rings=getPrimitiveRings(hbnList,maxDepth);
24     --- Does the ring analysis for quasi-two-dimensional ice
25     ringAnalysis(outDir, rings, hbnList, resCloud, maxDepth, confiningSheetArea);
26 end

```

Figure 2: The ‘lua’ input script, where the user is able to call any of the functions not voided by the options in the ‘YAML’ file.

Figure 2 shows a typical Lua input script, which calls functions exposed by the current YAML file work-flow.

2.3 YAML

```

1  trajectory: "../input/traj/dump.lammpstrj"
2  variables: "../lua_inputs/iceType/vars.lua"
3  bulk:
4      use: false
5      topologicalNetworkCriterion: false
6      bondOrderParameters: false
7  topoOneDim:
8      use: false
9  topoTwoDim:
10     use: true

```

Figure 3: The ‘YAML’ file, where boolean values are set to restrict functions exposed to the ‘lua’ scripting engine.

To improve usability and reduce the time required reading the API documentation, we have split the usage into a unique YAML-Lua design. The Lua interface is for power users, however, to reduce mistakes, options set in the YAML files will deactivate certain functions, in order to prevent incorrect manipulations of the internal data-structures. The YAML interface diverts the flow of functionality and code to different paths, and thus different algorithms. This also prevents name-clashes of similar functions for mutually exclusive work-flows. For example, an input system can either be a bulk system, a quasi-one-dimensional system or a quasi-two-dimensional system. The YAML file offers truthy options, an example of which is shown in Figure 3, and subsequently masks functions not applicable for the given system type.

3 Code Architecture

The work-flow pipeline is organized as follows:

- The user chooses whether the system is a bulk system, quasi-one-dimensional or quasi-two-dimensional system, by setting the appropriate values in the YAML input file (Figure 3).

- The Lua script (Figure 2) calls the functions to read in, analyze and output the desired results.
- Simulation data is read from LAMMPS trajectory files. The XYZ file format is also currently supported. Other file formats may be converted into an ASCII LAMMPS trajectory format [45].
- A common struct, the PointCloud structure, is used to hold the coordinate data of each frame.
- Options for controlling the output results can be specified in the Lua file input.
- Output directories are created automatically, according to the chosen work-flow, by Lua functions, which are present as a separate module.

```

119 // Struct that contains per-particle information
120 template <typename T> struct Point {
121     int type, molID, atomID; // type ID, molID, atomID
122     T x, y, z; // coordinates
123     std::vector<Result> c_ij; // Results (contains bond correlation type)
124     atom_state_type iceType =
125         molSys::unclassified; // Type of ice/water etc based on cij
126     bool inSlice = true; // Is the point inside the slice or not?
127 };
128
129 // Struct for a collection of points; contains information for a particular
130 // frame
131 template <typename S, typename T> struct PointCloud {
132     std::vector<S> pts; // Collection of points
133     int currentFrame; // Current frame number
134     int nop; // Number of atoms
135     std::vector<T> box; // Periodic box lengths
136     std::vector<T> boxLow; // xlo, ylo, zlo
137     std::unordered_map<int, int> idIndexMap;
138 };

```

Figure 4: The heart of the analysis code, PointCloud, an association of the Point structs, which is handled by safe memory access routines throughout the lifetime of the program.

The analysis of every work-flow in d-SEAMS utilizes a common PointCloud structure, as shown in Figure 4. This C++ struct is created for every frame, and contains the coordinates and basic simulation box data. Although most structural analyses require only the oxygen coordinates, analyses that depend on the HBN also require separate PointCloud structs for the hydrogen atoms.

3.1 Structural Identification Features

We are able to apply arbitrary transformations on the particle collections, in an efficient and idiomatic manner. Currently we have implemented the following structural schemes based on this easily extensible framework:

- The bond orientational parameters [46, 47], CHILL [48] and CHILL+ [49] parameters have been implemented. Clustering of ice-like molecules [50], based on these parameters can be optionally carried out by the user. The largest ice cluster so obtained can also be re-centered, for ease of visualization.
- Topological network criteria for bulk ice determination [30] have been implemented. d-SEAMS is able to identify and write out detailed information about Double-diamond cages (DDCs), hexagonal cages (HCs), and mixed rings for every frame. Additionally, the number of basal and prismatic rings are also computed.
- Primitive rings are identified. First, all possible rings are found using an exhaustive backtracking algorithm, following which non-shortest path rings are removed [29]. Ring networks with only hydrogen-bonded connections can be optionally determined.
- Confined quasi-two-dimensional ice classification by topological and graph theoretic approaches to the hydrogen-bonded ice-like particles.
- Quasi-one dimensional ice nano-tube (INT) and quasi-two-dimensional monolayer ice classification via topological network criteria [31]. The building blocks of n -gonal prismatic ice are explicitly and unequivocally identified.
- d-SEAMS is capable of calculating geometric order parameters for describing the phase transitions in confined ice.

4 Applications

Using d-SEAMS, structural and qualitative information as a time series can be easily obtained. This makes it possible to study a variety of diverse nucleating systems. Even the mechanism of nucleation growth can be inferred from an ensemble of trajectories, by analyzing the qualitative metrics supported by d-SEAMS.

4.1 Bulk Systems

4.1.1 Heterogenous Nucleation on an Ice-Promoting Surface

Silver iodide is an effective ice nucleating agent, whose lattice closely resembles that of bulk ice [51]. The smooth Ag-exposed β -AgI surface has been known to promote layer-by-layer growth of hexagonal ice (Ih) and cubic ice (Ic) in simulations [52]. Using d-SEAMS, we probe the underlying mechanism of the ice nucleation growth and behaviour. Ten independent simulations of 5120 TIP4P/Ice [53] molecules on a free-standing AgI surface were run upto ≈ 200 ns at 240 K. The simulation setup is similar to that of previous work in the literature [54].

Here we employ a topological network criterion [30] for identifying the building blocks of Ih and Ic, called hexagonal cages (HCs) and double-diamond cages (DDCs), respectively. Rings which belong to both HCs and DDCs are classified as mixed rings.

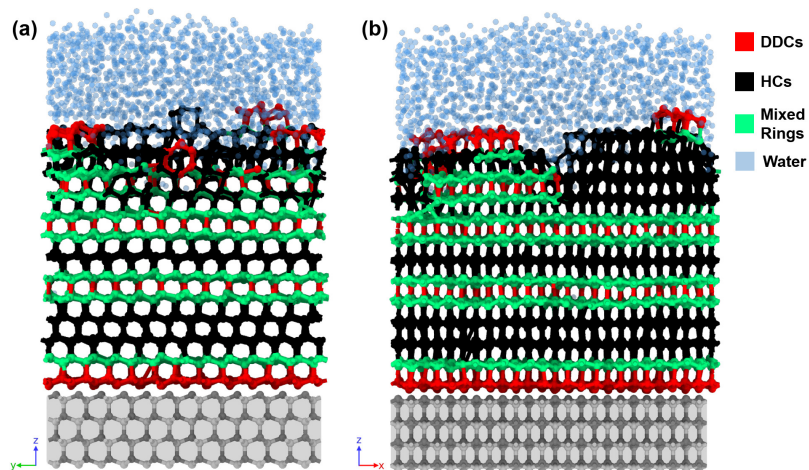


Figure 5: (a) YZ -plane and (b) XZ -plane views of layered hexagonal ice (Ih) and cubic ice (Ic) after 200 ns. DDCs, HCs and mixed rings are coloured in red, black and green, respectively. The silver and iodine atoms are dark-grey and grey respectively, with the AgI sheet highlighted in light grey.

Figure 5 depicts layers of HCs and DDCs, growing from the AgI surface, after 200 ns of simulation time. The close lattice match between the AgI surface and the ice phases is clearly visible. However, the CHILL algorithm [48] identifies the first layer of molecules close to the surface as liquid. It was noted in previous studies that although the CHILL algorithm does not identify the first layer of water molecules as ice, these molecules actually form part of the initial ice layer [52, 55]. The topological network criterion used here correctly classifies these water molecules as constituents of HCs or DDCs.

The Ag-exposed β -AgI surface supports the attachment of the basal plane of HCs, as well as DDCs. Figure 6 shows how layers grow through attachment of HCs and DDCs.

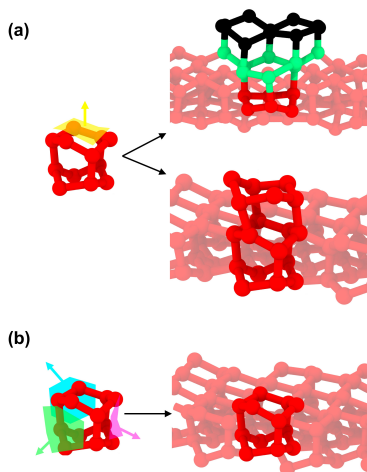


Figure 6: (a) Attachment of cages on the upper basal face of an HC. The basal face has been highlighted in yellow. Basal faces of an HC can support the growth of both DDCs (black) and HCs (red). (b) Attachment of HCs on the three prismatic faces, shaded in blue, green and mauve, of an HC. The prismatic faces of an HC cannot support the growth of DDCs. The colour scheme is the same as in Figure 5.

The peripheral rings of DDCs can support the attachment of both HCs and DDCs. However, the prismatic planes of an HC (highlighted in blue, green and mauve in Figure 6(b)) can only support the anchoring of HCs. Since the HCs grow upwards from the AgI surface, through the basal plane (highlighted in yellow in Figure 6(a)), only HCs can grow from the prismatic planes of pre-existing HCs in each layer. We surmise that the layer-wise growth of HCs in the lateral dimensions is because of this growth behaviour. This is in keeping with the stacking effects observed in the literature [54].

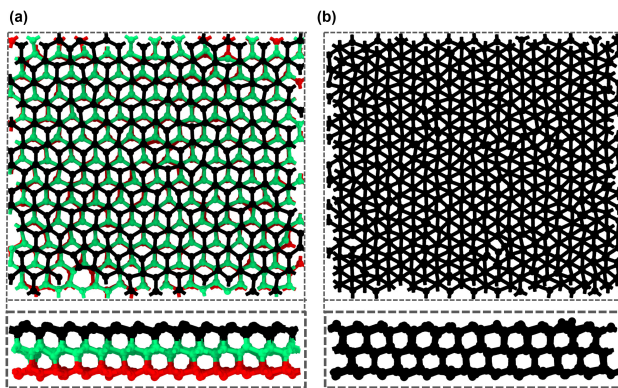


Figure 7: Overhead and side views showing the stacking arrangements of the first two layers of cages on the AgI surface, when more than half the water has been converted to ice, after more than ≈ 150 ns of simulation time. (a) The first layer is a layer of HCs. The complete second layer is a layer of DDCs in all cases observed. Mixed rings are sandwiched between the first layer of HCs and the second layer of DDCs. (b) The first and second layers are DDCs. The colour scheme is the same as in the preceding figures.

The effect of the surface is the most significant within the first two layers of cages. In all the independent trajectories, a single layer of either HCs or DDCs is formed first, upon which a second layer of DDCs grows. This stacking of cages is depicted visually in Figure 7. Regardless of the composition of the first two layers, alternating layers of varying widths of HCs and DDCs are formed in all the simulations. Interestingly, although HCs sometimes grow on the first layer, by the end of the simulations, the second layer is exclusively composed of DDCs.

We track the growth of the first two layers, with time, for a particular trajectory, whose stacking at the end of 200 ns is shown in Figure 7(a).

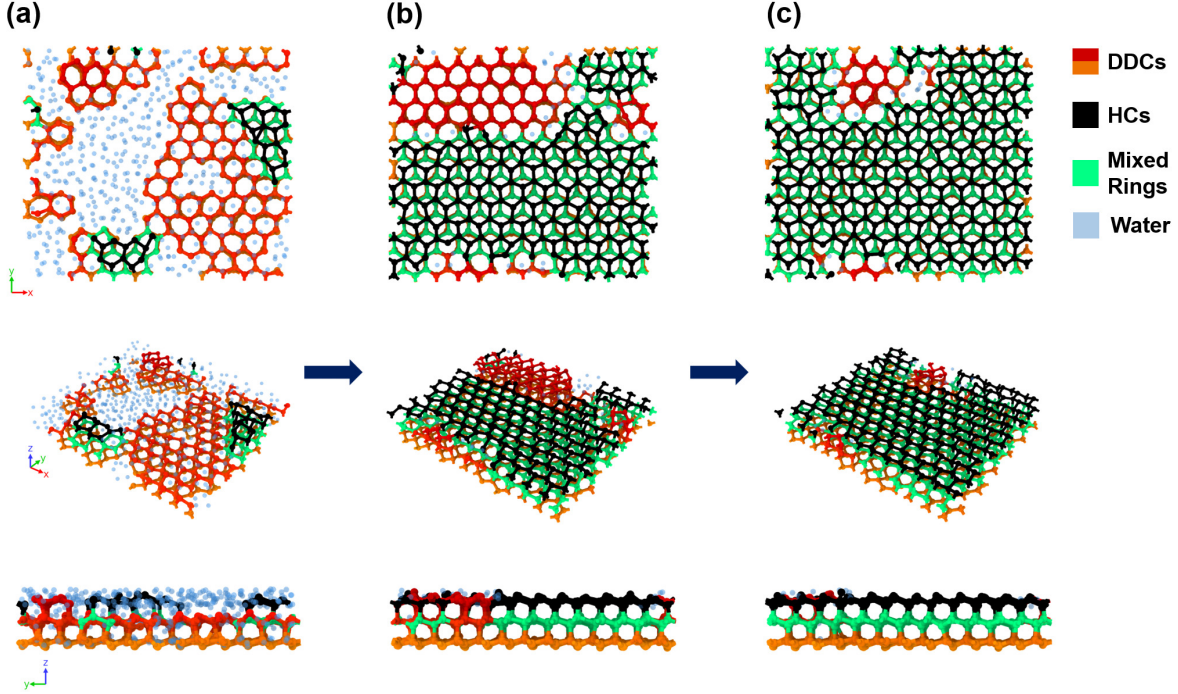


Figure 8: Formation of layers of HCs and DDCs within the first 100 *ns* of simulation time. (a) After ≈ 14 *ns*, the first layer has not completely formed. (b) After ≈ 60 *ns*, part of the second layer is comprised of HCs, and a separate portion of the second layer is composed of DDCs. The part of the second layer made up of HCs is distinguishable in the top view because of the AA-stacking order of HCs on the first layer of HCs. (c) After ≈ 100 *ns*, the second layer is almost entirely composed of DDCs. The colour scheme is shown in the legend. DDCs are coloured in shades of yellow to vermilion, according to the distance from the AgI surface.

Figure 8 shows the growth of the first two layers of cages within the first 100 *ns* of simulation time. After ≈ 60 *ns*, the second layer is partially composed of HCs and DDCs (Figure 8(b)). The HC portion is not anchored to the DDC part of the second layer, since DDCs cannot grow on the exposed lateral prismatic faces of the HCs. We note that eventually, by the time that the second layer of cages becomes continuous, HCs in the second layer disappear and are completely replaced by DDCs. In fact, the eventual layering of HCs and DDCs in the first two layers from the AgI surface is also observed on void-defect incorporated Ag-exposed β -AgI surfaces [54].

4.1.2 Homogenous Nucleation: Growth of the Largest Ice Cluster

Here, we have analyzed a trajectory which exhibits a successful homogenous nucleation event, in the bulk phase. Independent simulations of 4096 particles, modelled using the monoatomic water (mW) water model [56], were equilibrated at 300 *K* and quenched to 208 *K*. Simulations were subsequently run at constant temperature and pressure, in the NPT ensemble, at 1 *atm* and 208 *K* for upto 1 μ s. Figure 9 shows the structural features and growth of the largest ice cluster. In our ensemble of trajectories, we have observed that the largest ice crystallites which survive and grow to the post-critical size are rich in DDCs (shown in black in Figure 9). We find that even in post-critical crystallites, the core of the crystallites remains rich in DDCs. These findings match those gleaned from extensive forward-flux sampling simulations of both mW water and TIP4P/Ice [30]. The growth of the largest crystallite with time, showing fluctuations in the cluster size with time, is depicted in a supplementary movie, entitled `largestClusterGrowth.avi`, in the ESI (electronic supplementary information).

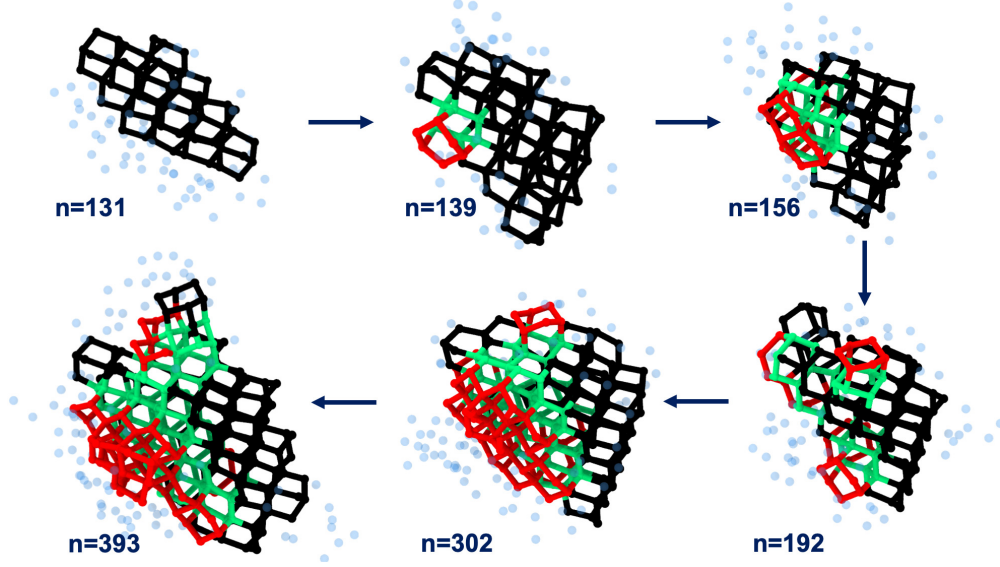


Figure 9: Evolution of an ice crystallite of mW water at 208 GPa in the NPT ensemble. DDCs are in black, HCs are in red and mixed rings belonging to both DDCs and HCs are in green. The number of particles in the largest cluster n is shown for every snapshot of the trajectory. Water molecules which do not participate in the cages are in transparent blue.

4.2 Quasi-Two-Dimensional Systems

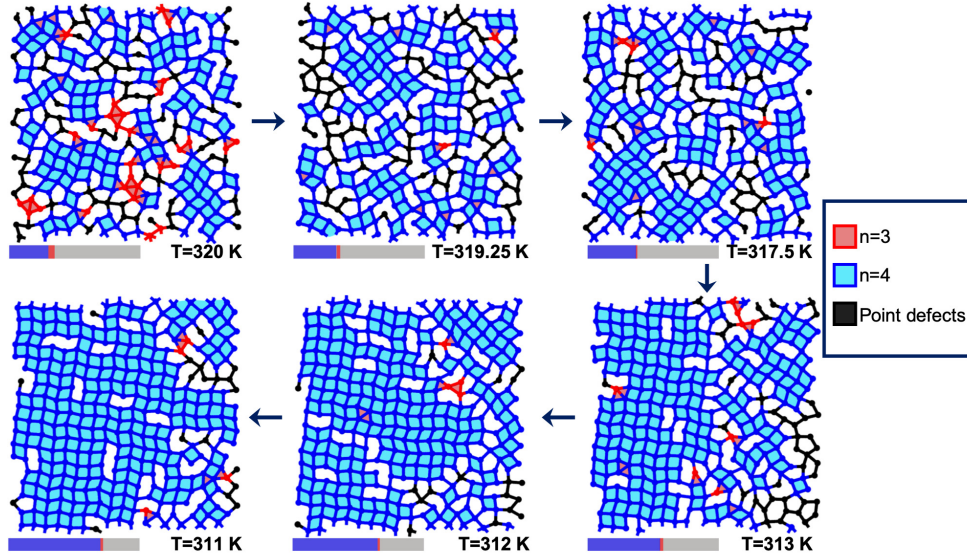


Figure 10: Snapshots of monolayer water being cooled from 320 K to 310 K , at 1 GPa . The stacked bars in the lower left corner of each snapshot denote the coverage area percentages for the 4-membered rings (blue) and 3-membered rings (red). The colours of the particles, bonds and interior ring shading are shown in the legend.

We further analyze Flat Monolayer Square Ice (fMSI), using d-SEAMS. FMSI has been observed in simulations, when water subjected to a lateral pressure of 1 GPa is sandwiched between rigid graphene sheets, separated by a slit width of 6 Å [18, 57]. d-SEAMS is capable of calculating the coverage area metric [31], an area-based order parameter, at every timestep of a trajectory. We demonstrate the efficacy of the coverage area metric in describing phase transitions, during the cooling of a quasi-two-dimensional monolayer from 320 K to 310 K over 1 ns . The visuals produced were generated from the output of d-SEAMS. Figure 10 shows snapshots of the monolayer water through various stages of

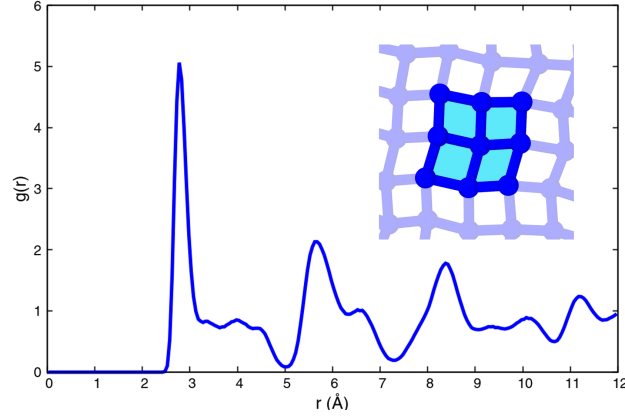


Figure 11: In-plane oxygen-oxygen radial distribution function of the ice formed at 310 K and $P_{xx} = 1$ GPa . The inset shows the 4-membered rings characteristic of fMSI.

cooling, exhibiting a gradual increase in the proportion of the 4-membered rings. At 320 K , the coverage area of the 4-membered rings is $\approx 70\%$, which indicates that the monolayer is predominantly fMSI. This phase change is depicted in a supplementary video (`monolayer.avi`) in the ESI.

d-SEAMS is also capable of calculating the in-plane radial distribution function. The solid-like ordered nature of the ice formed at 310 K is typified by the shape of the 2-dimensional oxygen-oxygen radial distribution function in Figure 11. The $g_{OO}(r)$ has the highest peak at 2.775 ± 0.05 Å, followed by a shoulder peak and a third smaller peak; the same features have been previously observed for fMSI. The frames were obtained from an equilibrated 1 ns run at a constant temperature of 310 K and lateral pressure of 1 GPa .

Table 1: Ring statistics and Coverage Area percentage for triangular and square ices

Number of nodes	Coverage Area _n %	Number of rings
n=4	74.422 ± 3.345	238.94 ± 10.723
n=3	0.877 ± 0.5	6.2 ± 3.544

Figure 1 summarizes the ring statistics and coverage area metric values, determined by d-SEAMS, for the fMSI structure formed at 310 K . The coverage area metric is a more intuitive and more stable metric than the number of rings, as is evident from the data. The number of rings is more sensitive to small thermal fluctuations which are not relevant to the overall classification scheme.

4.3 Quasi-One-Dimensional Systems

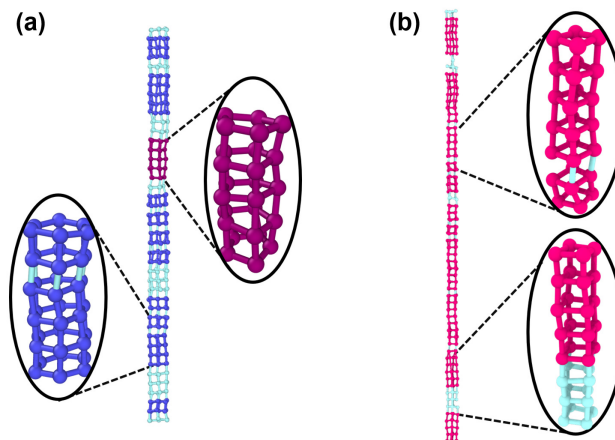


Figure 12: View of ice structures at 240K confined within (a) (10,0) zig-zag nanotube at 0.1MPa and (b) (11,0) zig-zag nanotube at 1MPa. The unclassified phase, either water or deformed prism blocks, is sea-green. Prism blocks of pentagonal, hexagonal, and tetragonal ices are shown in purple, blue and pink respectively.

Figure 12(b) shows the (11, 0) SWCT, subjected to an axial pressure of $P_{zz} = 1 \text{ MPa}$. Under these conditions, the INT is predominantly comprised of tetragonal prism blocks, with intermittent deformed prism blocks.

The length of the INT in Figure 12(a) is smaller than that in Figure 12(b). The number of prism blocks of each type is an unreliable indicator, which does not qualitatively describe the relative proportions of the prismatic ice phases. Although a volume-based metric has been proposed [31], an approximate metric based on the normalized number of prism blocks may be used as a reasonable approximation of relative proportion.

We have observed that the average height of each prism block remains relatively constant at a value of $\approx 2.845 \pm 0.07$ Å, irrespective of the number of nodes in the basal ring (n) and even the applied pressure P_{zz} . Therefore, it is possible to define a theoretical maximum possible number of n -gonal prism blocks, assuming that the entire SWCT height is filled with n -gonal prism blocks, each of height ≈ 2.845 Å. Since the average height of the prism blocks is independent of n , the theoretical maximum number of prism blocks is the same for all n . The theoretical maximum number of prism blocks N_{max} is thus:

$$N_{max} = \frac{H_{SWCT}}{h_{avg}}$$

where H_{SWCT} is the height of the SWCT; $h_{avg} = 2.845$ is the average height of the prism blocks. Both measurements are in Å.

The normalized $height_n\%$ for any prismatic ice phase is defined as follows:

$$Height_n\% = \frac{N_n}{N_{max}} \times 100$$

where, N_{max} is the theoretical maximum possible number of n -gonal prism blocks; N_n is the actual number of n -gonal prism blocks.

Table 2 summarizes the relative proportions of the n -gonal prism blocks for the SWCTs. N_{max} is the same for every n , and thus the (11,0) and (13,0) SWCTs have $N_{max} = 63.492\%$ and $N_{max} = 43.207\%$, respectively, for all n . It is evident that the normalized height percentage matches reasonably well with the occupied volume percentage.

Table 2: Relative proportions of n -gonal prism blocks

SWCT Type	Actual Number (N_n)	Maximum Number (N_{max})	Normalized Height % (H_n)	Occupied Volume % (V_n)
(11, 0) SWCT	$N_4 = 40$	$N_{max} = 63.627$	$H_4 = 63.492\%$	$V_4 = 69.611\%$
(13, 0) SWCT	$N_5 = 4$ $N_6 = 16$	$N_{max} = 43.207$	$H_5 = 9.302\%$ $H_6 = 37.21\%$	$V_5 = 9.658\%$ $V_6 = 42.982\%$

4.3.1 Freezing of an Ice Nanotube

We track the phase change from the liquid to solid state in water confined within a (13,0) featureless nanotube, approximating a zigzag carbon nanotube. The temperature is lowered in steps of 10 K . Simulations are run in the $NP_{zz}T$ ensemble for 20 ns at each temperature, subjected to a constant pressure of 0.5 MPa at each temperature for 20 ns .

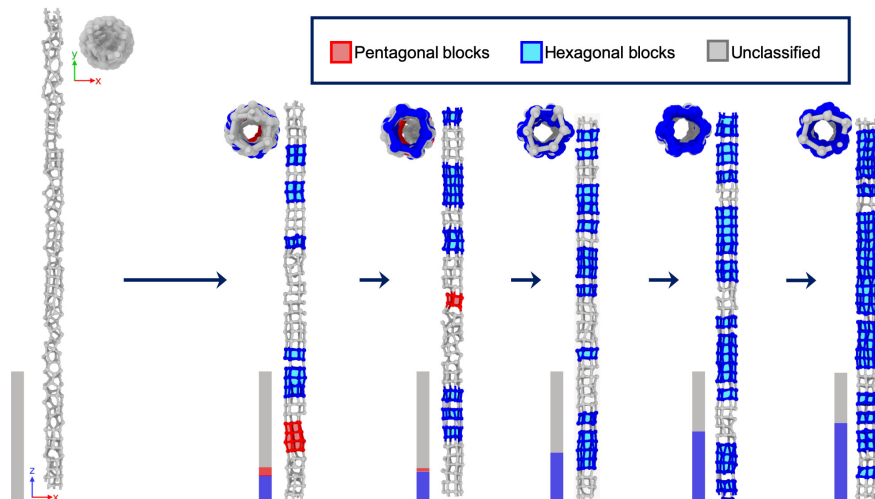


Figure 13: Snapshots of an icy nanoribbon at various timesteps, at 280 K and $P_{zz} = 0.5\text{ MPa}$, in a $(13, 0)$ smooth single-walled nanotube. The stacked bars in the lower left corner of each snapshot denote the height percentages for the dominant phases: hexagonal prism blocks (blue) and pentagonal prism blocks (red). Initially, the quasi-one-dimensional water is entirely in the liquid phase.

We observe an abrupt change in phase from the liquid state to ordered prismatic ice phase at a temperature of 280 K . In the previous section, we showed how the $height_n\%$ metric matches well with the occupied volume percentage, which has been proven to be an effective order parameter for nucleating quasi-one-dimensional systems [31]. Thus, the phase change of an INT can be described by the $height_n\%$ order parameter. Figure 13 depicts the phase change from the liquid phase, at the beginning of the simulation, to $\approx 60\%$ hexagonal prismatic phase after the 20 ns simulation time. The dominant ice phase formed is the hexagonal prismatic phase, with small proportions of pentagonal ice (within $7\text{ }height_5\%$).

A movie (entitled `intEvol.avi` in the ESI) documents this phase change.

5 Conclusion

d-SEAMS is a flexible post-processing analysis tool, capable of classifying water at both extremes of scale: highly confined systems as well as bulk water. d-SEAMS is the first scientific software to use `nix` as a packaging manager to circumvent dependency clashes. d-SEAMS is built as a functional `nix`-derivation, making it easy to interface with foreign libraries, and ensuring complete reproduction of the developers' build-environment on a variety of operating systems. The Lua scripting interface, as well as the C++ API are meant to provide enough rigor for developers while being easy to use for the general scientific community.

Several applications of qualitative analysis have been presented. We have shown how d-SEAMS is capable of determining the time evolution of structures, from which the growth mechanism and new physical insights have been inferred for heterogeneous nucleation. A new order parameter for determining the relative composition of n -gonal ice in quasi-one-dimensional nanotubes has been formulated and implemented. The new order parameter, the $height\%$, produces results that match well with previously defined metrics in the literature. We have demonstrated the versatility of d-SEAMS by performing detailed structural analysis for homogenous nucleation, fMSI formation and ice nanotube freezing from the liquid state.

d-SEAMS (<https://dseams.info>) is a free and open-source molecular dynamics engine, distributed on GitHub under the GNU General Public License and documented online (<https://docs.dseams.info>). We envisage future development to incorporate more input formats and structural analysis algorithms. Given the nature of the engine, we expect additions to the framework which would provide insights into biomolecular systems as well.

6 Acknowledgments

The computational resources were provided by the HPC facility of the Computer Center(CC), Indian Institute of Technology Kanpur. R.G. acknowledges the invaluable support of his lab PI, D. Goswami.

References

1. Petrenko, V. & Whitworth, R. *Physics of Ice*. Oxford Univ 2002.
2. Salzmann, C. G., Hallbrucker, A., Finney, J. L. & Mayer, E. Raman spectroscopic study of hydrogen ordered ice XIII and of its reversible phase transition to disordered ice V. *Physical Chemistry Chemical Physics* **8**, 3088 (2006).
3. Salzmann, C. G., Hallbrucker, A., Finney, J. L. & Mayer, E. Raman spectroscopic features of hydrogen-ordering in ice XII. *Chemical Physics Letters* **429**, 469–473 (Oct. 2006).
4. Salzmann, C. G., Radaelli, P. G., Mayer, E. & Finney, J. L. Ice XV: A New Thermodynamically Stable Phase of Ice. *Physical Review Letters* **103** (Sept. 2009).
5. Falenty, A., Hansen, T. C. & Kuhs, W. F. Formation and properties of ice XVI obtained by emptying a type sII clathrate hydrate. *Nature* **516**, 231–233 (Dec. 2014).
6. Del Rosso, L., Celli, M. & Ulivi, L. New porous water ice metastable at atmospheric pressure obtained by emptying a hydrogen-filled ice. *Nature Communications* **7** (Nov. 2016).
7. Algara-Siller, G. *et al.* Square ice in graphene nanocapillaries. *Nature* **519**, 443–445 (Mar. 2015).
8. Agrawal, K. V., Shimizu, S., Drahushuk, L. W., Kilcoyne, D. & Strano, M. S. Observation of extreme phase transition temperatures of water confined inside isolated carbon nanotubes. *Nature Nanotechnology* **12**, 267–273 (Nov. 2016).
9. Zhao, W.-H., Bai, J., Yuan, L.-F., Yang, J. & Zeng, X. C. Ferroelectric hexagonal and rhombic monolayer ice phases. *Chem. Sci.* **5**, 1757–1764 (2014).
10. Takaiwa, D., Hatano, I., Koga, K. & Tanaka, H. Phase diagram of water in carbon nanotubes. *Proceedings of the National Academy of Sciences* **105**, 39–43 (Dec. 2007).
11. Bai, J., Angell, C. A. & Zeng, X. C. Guest-free monolayer clathrate and its coexistence with two-dimensional high-density ice. *Proceedings of the National Academy of Sciences* **107**, 5718–5722 (Mar. 2010).
12. Salzmann, C. G., Radaelli, P. G., Slater, B. & Finney, J. L. The polymorphism of ice: five unresolved questions. *Physical Chemistry Chemical Physics* **13**, 18468 (2011).
13. Salzmann, C. G. Advances in the experimental exploration of water’s phase diagram. *The Journal of Chemical Physics* **150**, 060901 (Feb. 2019).
14. Chen, J., Schusteritsch, G., Pickard, C. J., Salzmann, C. G. & Michaelides, A. Two Dimensional Ice from First Principles: Structures and Phase Transitions. *Physical Review Letters* **116** (Jan. 2016).
15. Koga, K., Tanaka, H. & Zeng, X. C. First-order transition in confined water between high-density liquid and low-density amorphous phases. *Nature* **408**, 564–567 (Nov. 2000).
16. Zangi, R. & Mark, A. E. Monolayer Ice. *Physical Review Letters* **91** (July 2003).
17. Bai, J. & Zeng, X. C. Polymorphism and polyamorphism in bilayer water confined to slit nanopore under high pressure. *Proceedings of the National Academy of Sciences* **109**, 21240–21245 (Dec. 2012).
18. Zhu, Y., Wang, F., Bai, J., Zeng, X. C. & Wu, H. Compression Limit of Two-Dimensional Water Constrained in Graphene Nanocapillaries. *ACS Nano* **9**, 12197–12204. ISSN: 1936-0851 (Dec. 22, 2015).
19. Zhu, Y., Wang, F., Bai, J., Zeng, X. C. & Wu, H. Formation of Trilayer Ices in Graphene Nanocapillaries under High Lateral Pressure. *The Journal of Physical Chemistry C* **120**, 8109–8115 (Apr. 2016).
20. Gao, Z., Giovambattista, N. & Sahin, O. Phase Diagram of Water Confined by Graphene. *Sci Rep* **8**, 1–11. ISSN: 2045-2322 (Apr. 18, 2018).
21. Boettiger, C. An introduction to Docker for reproducible research. *ACM SIGOPS Operating Systems Review* **49**, 71–79 (Jan. 2015).
22. Michaud-Agrawal, N., Denning, E. J., Woolf, T. B. & Beckstein, O. MDAAnalysis: A toolkit for the analysis of molecular dynamics simulations. *Journal of Computational Chemistry* **32**, 2319–2327 (Apr. 2011).
23. McGibbon, R. *et al.* MDTraj: A Modern Open Library for the Analysis of Molecular Dynamics Trajectories. *Biophysical Journal* **109**, 1528–1532 (Oct. 2015).
24. Humbert, M. T., Zhang, Y. & Maginn, E. J. PyLAT: Python LAMMPS Analysis Tools. *Journal of Chemical Information and Modeling* **59**, 1301–1305 (Mar. 2019).
25. Guo, P. J. *CDE: Run Any Linux Application On-Demand Without Installation*. in *LISA* (2011).
26. Tauber, T. *When importless becomes meaningful* in *Proceedings of the companion publication of the 2014 ACM SIGPLAN conference on Systems, Programming, and Applications: Software for Humanity - SPLASH ’14* (ACM Press, 2014).
27. Dolstra, E., de Jonge, M. & Visser, E. Nix: A Safe and Policy-Free System for Software Deployment, 15 (2004).

28. Prins, J., Suresh, J. & Dolstra, E. *Nix fixes dependency hell on all Linux distributions* in *Linux* (2008).
29. Franzblau, D. S. Computation of ring statistics for network models of solids. *Physical Review B* **44**, 4925–4930 (Sept. 1991).
30. Haji-Akbari, A. & Debenedetti, P. G. Direct Calculation of Ice Homogeneous Nucleation Rate for a Molecular Model of Water. *Proceedings of the National Academy of Sciences* **112**, 10582–10588. ISSN: 0027-8424, 1091-6490 (Aug. 25, 2015).
31. Goswami, A. & Singh, J. K. A General Topological Network Criterion for Exploring the Structure of Icy Nanoribbons and Monolayers. *Physical Chemistry Chemical Physics* (2019).
32. Stukowski, A. Visualization and analysis of atomistic simulation data with OVITO—the Open Visualization Tool. *Modelling and Simulation in Materials Science and Engineering* **18**, 015012 (Dec. 2009).
33. Humphrey, W., Dalke, A. & Schulten, K. VMD: Visual molecular dynamics. *Journal of Molecular Graphics* **14**, 33–38 (Feb. 1996).
34. Stallman, R., Pesch, R., Shebs, S., *et al.* Debugging with GDB. *Free Software Foundation* **51**, 02110–1301 (2002).
35. Dolstra, E., Löh, A. & Pierron, N. NixOS: A Purely Functional Linux Distribution. *Journal of Functional Programming* **20**, 577–615. ISSN: 1469-7653, 0956-7968 (Nov. 2010).
36. Peng, R. D. Reproducible Research in Computational Science. *Science* **334**, 1226–1227. ISSN: 0036-8075, 1095-9203 (Dec. 2, 2011).
37. Plimpton, S. Fast Parallel Algorithms for Short-Range Molecular Dynamics, 42.
38. Abraham, M. J. *et al.* GROMACS: High Performance Molecular Simulations through Multi-Level Parallelism from Laptops to Supercomputers. *SoftwareX* **1-2**, 19–25. ISSN: 2352-7110 (Sept. 1, 2015).
39. McGibbon, R. T. *et al.* MDTraj: A Modern Open Library for the Analysis of Molecular Dynamics Trajectories. *Biophysical Journal* **109**, 1528–1532. ISSN: 0006-3495 (Oct. 20, 2015).
40. Weik, F. *et al.* ESPResSo 4.0 – an Extensible Software Package for Simulating Soft Matter Systems. *Eur. Phys. J. Spec. Top.* **227**, 1789–1816. ISSN: 1951-6401 (Mar. 1, 2019).
41. Giannozzi, P. *et al.* QUANTUM ESPRESSO: A Modular and Open-Source Software Project for Quantum Simulations of Materials. *J. Phys.: Condens. Matter* **21**, 395502. ISSN: 0953-8984 (Sept. 2009).
42. Oliphant, T. E. Python for Scientific Computing. *Computing in Science Engineering* **9**, 10–20. ISSN: 1521-9615 (May 2007).
43. Walt, S. van der, Colbert, S. C. & Varoquaux, G. The NumPy Array: A Structure for Efficient Numerical Computation. *Computing in Science Engineering* **13**, 22–30. ISSN: 1521-9615 (Mar. 2011).
44. Stallman, R., Pesch, R. & Shebs, S. Debugging with GDB, 352.
45. Shirts, M. R. *et al.* Lessons learned from comparing molecular dynamics engines on the SAMPL5 dataset. *Journal of Computer-Aided Molecular Design* **31**, 147–161 (Oct. 2016).
46. Steinhardt, P. J., Nelson, D. R. & Ronchetti, M. Bond-orientational order in liquids and glasses. *Physical Review B* **28**, 784–805 (July 1983).
47. Ten Wolde, P. R., Ruiz-Montero, M. J. & Frenkel, D. Numerical calculation of the rate of crystal nucleation in a Lennard-Jones system at moderate undercooling. *The Journal of Chemical Physics* **104**, 9932–9947 (June 1996).
48. Moore, E. B., de la Llave, E., Welke, K., Scherlis, D. A. & Molinero, V. Freezing, Melting and Structure of Ice in a Hydrophilic Nanopore. *Physical Chemistry Chemical Physics* **12**, 4124. ISSN: 1463-9076, 1463-9084 (2010).
49. Nguyen, A. H. & Molinero, V. Identification of Clathrate Hydrates, Hexagonal Ice, Cubic Ice, and Liquid Water in Simulations: The CHILL+ Algorithm. *The Journal of Physical Chemistry B* **119**, 9369–9376. ISSN: 1520-6106, 1520-5207 (July 23, 2015).
50. Stoddard, S. D. Identifying clusters in computer experiments on systems of particles. *Journal of Computational Physics* **27**, 291–293 (May 1978).
51. Vonnegut, B. The Nucleation of Ice Formation by Silver Iodide. *Journal of Applied Physics* **18**, 593–595 (July 1947).
52. Zielke, S. A., Bertram, A. K. & Patey, G. N. A Molecular Mechanism of Ice Nucleation on Model AgI Surfaces. *The Journal of Physical Chemistry B* **119**, 9049–9055 (Oct. 2014).
53. Abascal, J. L. F., Sanz, E., Fernández, R. G. & Vega, C. A potential model for the study of ices and amorphous water: TIP4P/Ice. *The Journal of Chemical Physics* **122**, 234511 (June 2005).
54. Prerna, Goswami, R., Metya, A. K., Shevkunov, S. V. & Singh, J. K. Study of Ice Nucleation on Silver Iodide Surface with Defects. *Molecular Physics*, 1–13. ISSN: 0026-8976, 1362-3028 (Aug. 25, 2019).
55. Zielke, S. A., Bertram, A. K. & Patey, G. N. Simulations of Ice Nucleation by Model AgI Disks and Plates. *The Journal of Physical Chemistry B* **120**, 2291–2299 (Feb. 2016).

56. Molinero, V. & Moore, E. B. Water Modeled As an Intermediate Element between Carbon and Silicon†. *The Journal of Physical Chemistry B* **113**, 4008–4016 (Apr. 2009).
57. Yang, L., Guo, Y. & Diao, D. Structure and dynamics of water confined in a graphene nanochannel under gigapascal high pressure: dependence of friction on pressure and confinement. *Physical Chemistry Chemical Physics* **19**, 14048–14054 (2017).